E-Link: A 256-ch Mini-Pedestal Connector for High-Density Soft Neural Interfaces

Tianyu Bai, Gen Li, Yongli Qi, and Hui Fang

***Abstract*—High-density thin-film neural interfaces face persistent packaging challenges at the electrode–electronics interface, where conventional rigid connectors impose high insertion forces, strict alignment requirements, and limited reusability. We present E-Link (Elastomeric Link), a modular 256-channel mini-pedestal connector designed to facilitate simplified, user-friendly assembly through an insertion-free, alignment-tolerant interface utilizing an elastomeric conductive interposer and a compliant threaded compression mechanism. Finite element analysis and experimental validation confirm uniform contact stress across the 16 × 16 interconnect array. The system achieves stable electrical performance, exhibiting contact impedances of 0.3-0.4 kΩ, an RMS noise floor of 2.68 ± 0.46 μV, and a connection yield exceeding 97% over 100 mating cycles. The detachable architecture reduces chronic head-mounted mass from 6.6 g to 2.8 g while maintaining safe thermal operation (30.5 °C steady-state) under a full 20 kHz sampling bandwidth. Design analysis further indicates scalability toward 1024-channel integration within the same 25-mm-diameter footprint by leveraging fine-pitch elastomeric conductive pillars. This work provides a robust and scalable connection solution for high-density flexible neural interfaces with broad application for bioelectronics.**

***Index Terms*—Elastomeric conductive interposer, high-density interconnects, low-noise neural recording, neural implants, thin-film microelectrode arrays.**

I. INTRODUCTION

THE development of thin-film, polymer-based neural interfaces has fundamentally advanced neural recording and stimulation by enabling high spatial resolution and improved biocompatibility, aligning closely with the core objectives of flexible electronics and microsystems for chronic biointegration. These flexible interfaces, including electrocorticography (ECoG) arrays, intracortical microelectrode arrays, and peripheral nerve interfaces, have become indispensable devices and tools for brain–computer interfaces (BCIs), systems neuroscience, and translational neuroengineering [1].

As neural interface technologies mature, the field is rapidly progressing toward high-channel-count systems (hundreds to thousands of channels and beyond), driven by demands for higher information throughput, improved decoding accuracy, and increased precision in therapies [1], [2]. While substantial efforts have optimized electrode materials, geometries, and surface chemistries, long-term system performance is no longer limited only by the electrode–tissue interface [3]. Instead, another dominant bottleneck for chronic deployment now resides at the system-integration level, specifically, in the mechanical and electrical packaging that bridges soft, high-density neural electrodes with rigid signal-processing electronics.

This soft–hard interface presents a uniquely challenging engineering problem. Flexible thin-film electrodes are mechanically soft, highly deformable, and highly sensitive to misalignment, whereas backend electronics demand stable, repeatable, and low-impedance electrical connections. In practice, failures at this interface frequently dictate overall system lifetime, even when the implanted electrode array remains electrically functional. Consequently, connector reliability, mechanical compliance, and modularity have emerged as critical, yet often underappreciated, determinants of chronic neural recording success.

Conventional approaches for interfacing high-channel-count neural probes with electronic headstages rely predominantly on micro-miniature rigid connectors, such as Omnetics or Hirose series [4], [5]. These pin-based connectors provide excellent electrical performance at modest channel counts and have become the established industry standard for acute and short-term experiments. However, their scalability is fundamentally constrained. As channel count increases, the required insertion force rises proportionally, substantially elevating the risk of mechanical damage to thin-film traces, solder joints, or cranial mounting structures. Moreover, the reliance on precise pin-to-socket alignment renders these connectors highly susceptible to failure from even sub-millimeter misalignment, leading to bent pins, intermittent contacts, or catastrophic shorts.

Beyond alignment and insertion force limitations, the rigid, bulky form factors of traditional connectors introduce additional challenges for chronic implantation. Increased connector height and head-mounted mass amplify bending moments at the implant site and increase skin strain, potentially leading to skin erosion, infection, and implant instability. In freely behaving animal models, excessive head-mounted weight has been shown to alter natural behaviors and introduce

Manuscript received Jan 31, 2026; revised Mar 27, 2026; accepted xxx xx, 2026. Date of publication xxx xx, 2026; date of current version xxx xx, 2026. This work was supported in part by the National Institutes of Health under Grant R01MH139342 and in part by the Dartmouth PhD Innovation Fellowship. *(Corresponding author: Hui Fang).*

The authors are with the Multifunctional Integrated NeuroElectronics (MINE) Lab, Thayer School of Engineering, Dartmouth College, Hanover, NH 03755 USA (e-mail: hui.fang@dartmouth.edu).

The complete structure and the intuitive mating process are further illustrated in Video S1 (animated full-rotation structural overview) and Video S2 (assembly/disassembly procedures) in the supplemental materials.

All design files, fabrication documentation, and assembly instructional videos supporting this work are available in an open-source repository on GitHub at https://github.com/Tianyu-Bai/E-Link

Digital Object Identifier xx.xxxx/JFLEX.2026.xxxxxxx

motion-related artifacts that degrade recording quality [6]. Collectively, these limitations restrict the practicality of rigid connectors for long-term, high-density neural recording.

To reduce the mechanical footprint of rigid connectors, several low-profile interconnection strategies have been explored, including anisotropic conductive film (ACF) bonding and direct ultrasonic or thermocompression welding to amplifier boards [7], [8], [9]. While these approaches reduce connector height and eliminate pin-alignment requirements, they introduce distinct trade-offs. Most notably, they are inherently permanent or semi-permanent, precluding routine detachment of backend electronics from the implanted electrode array. This lack of modularity hinders the reuse of costly signal-processing hardware and complicates maintenance, troubleshooting, and system upgrades [4]. In many cases, failure of a single interconnect necessitates replacing the entire implanted array, increasing experimental costs and animal burden.

Existing interconnection strategies thus expose a fundamental limitation in chronic neural interface design towards achieving simultaneously high channel density, low electrical noise, mechanical compliance, and modular reusability at the soft–hard interface. An ideal solution must tolerate mechanical misalignment, minimize insertion forces, distribute contact stress uniformly across fragile thin-film electrodes, and support repeated connection cycles without degradation of electrical performance, all while maintaining a compact, lightweight form factor suitable for chronic implantation [10].

In this work, we present a modular 256-channel mini-pedestal connector that addresses these challenges through an insertion-free, alignment-tolerant interconnection architecture specifically designed for flexible neural interfaces. The system employs an elastomeric conductive interposer combined with a compliant threaded compression mechanism to achieve uniform, low-impedance electrical contact across a 16 × 16 channel array without precision pin alignment or permanent bonding. Through finite element modeling and comprehensive electrical, thermal, and mechanical characterization, we demonstrate stable low-noise performance, robust durability over repeated mating cycles, and reduced chronic head-mounted mass. The underlying design principles further support scalability toward higher channel counts, providing a generalizable packaging framework for next-generation flexible bioelectronic systems.

II. System Architecture And Mechanical Design

A. Modular Mini-Pedestal Design Concept

The proposed 256-channel connector is designed as a modular mini-pedestal-and-cap architecture that decouples the mechanically fragile electrode–tissue interface from the comparatively heavy signal-processing electronics [11]. As illustrated in the exploded view in Fig. 1(a), the assembly comprises a threaded mini-pedestal (⑧) affixed to the surgical site, which houses both the adapter printed circuit board (PCB) (⑥) and the polymer-based neural interface (⑦).

A customized 256-channel headstage (④) is positioned above the mini-pedestal and electrically interfaced through a conductive pillar–embedded elastomeric interposer (⑤), enabling insertion-free, high-density electrical contact. The entire assembly is mechanically secured by a threaded cap (①) integrated with a compliant foam washer (②), which provides controlled compression and ensures stable mechanical interlocking under repeated attachment cycles.

This modular configuration is a critical design feature for chronic implantation. By allowing the headstage electronics to be detached during non-recording periods, the system reduces the head-mounted mass from 6.6 g to 2.8 g, thereby minimizing chronic mechanical load on the implant site, reducing biological stress, and enabling efficient reuse of backend recording hardware.

B. Mechanical Interlocking and Compression Strategy

The mechanical reliability of the 256-channel interface is enabled by a controlled compression strategy that eliminates the need for conventional high-density pin-based connectors, which are inherently susceptible to misalignment and mechanical damage. As illustrated in the cross-sectional view in Fig. 1(b), the system leverages the mechanical advantage of a threaded interface to achieve secure and repeatable electrical interconnection.

In this configuration, the adapter PCB (⑥) is precisely seated on an internal step within the mini-pedestal (⑧), establishing a well-defined axial reference plane. When manual torque is applied to the threaded cap (①), a uniform downward axial force is generated and transmitted through a compliant foam washer (②) to the customized headstage (④). To ensure long-term electronic reliability, headstage components interfacing with the foam washer are encapsulated with a transparent, waterproof potting compound that mechanically isolates sensitive circuitry and enables uniform pressure distribution. The applied axial compression uniformly compresses the elastomeric conductive interposer (⑤), thereby establishing stable, insertion-free electrical connections between the headstage (④) and the adapter PCB (⑥). This approach is optimally designed for chronic neural implants, as it provides a robust, self-aligning mating mechanism that preserves signal integrity across hundreds of channels while avoiding the high insertion forces associated with rigid plug-based connectors.

The cross-sectional architecture further incorporates a dedicated floating cavity to accommodate the elastomeric interposer (⑤). As the headstage PCB is driven downward by the threaded cap, this cavity allows controlled compression of the elastomer between the two PCB planes. To standardize compression without external tools, engineered thread positions provide a visual calibration, aligning explicit 'F' (Front) and 'R' (Right) marks on the housing for optimal mating (Fig. 1). In combination with the mini-pedestal step that constrains the adapter PCB, this structural arrangement ensures uniform contact pressure and consistent electrical engagement across the full channel array. Collectively, these features yield a compliant interconnection architecture that tolerates positional misalignment and supports long-term, high-density neural recording.

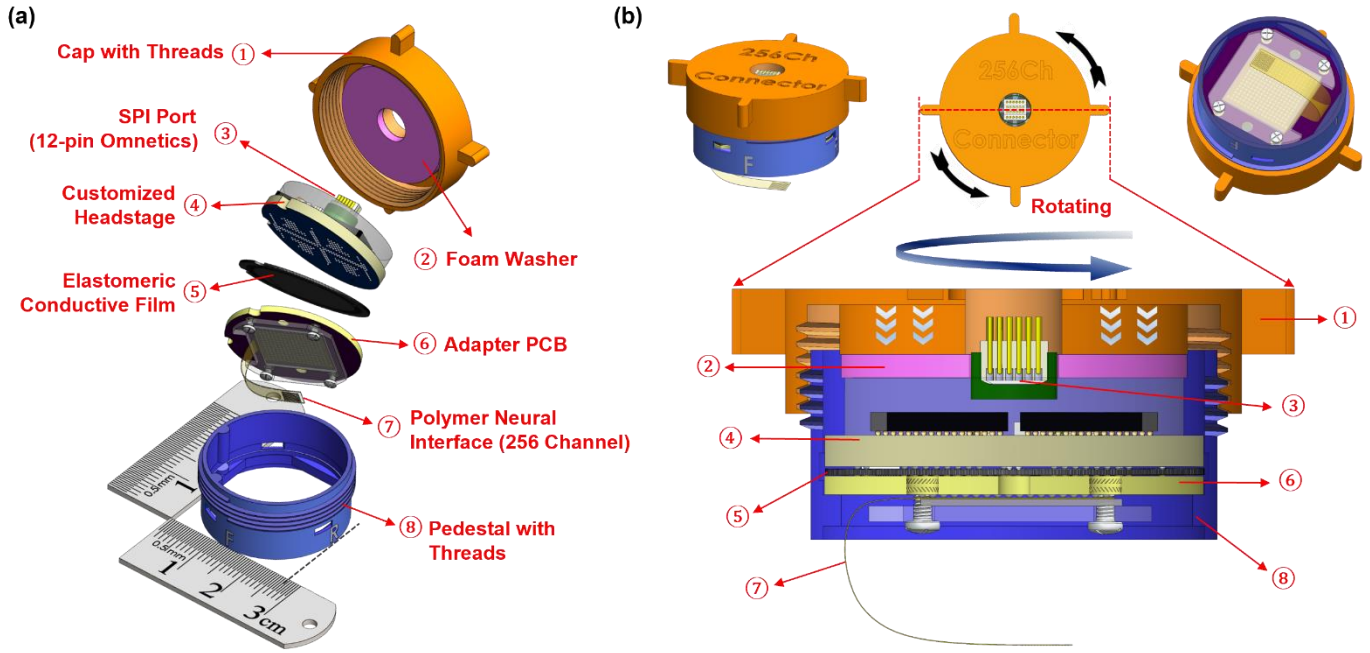

Fig. 1. System design concept and mechanical integration strategy. (a) Exploded-view schematic illustrating the assembly components of the modular 256-channel pedestal connector. The system integrates a polymer neural interface with a customized headstage using an elastomeric interposer. (b) Fully assembled connector: side view (top left), top view (top middle), and bottom view (top right). The bottom panel provides a cross-sectional view of the threaded compression mechanism. The housing design converts manual torque into uniform axial pressure, facilitating stable electrical interlocking between the adapter PCB which is fixed on the internal pedestal step and headstage contacts without the need for precision pin alignment.

C. Thin-Film Probe and Adapter Board Sandwich Integration

The transition from the flexible polyimide thin-film probe to the rigid adapter PCB is realized through a precision-engineered sandwich assembly, as highlighted in the upper-right detail of Fig. 1(b). To maintain an ultra-low-profile form factor and ensure a flush mechanical interface, four M1.2 micro-knurled nuts with a height of 1.0 mm are press-fitted into pre-drilled apertures (1.18 mm in diameter) on the 1.2 mm thick adapter PCB. This specific tolerance allows the nuts to be fully recessed within the PCB substrate, eliminating vertical protrusions that could interfere with overall headstage seating.

The structural transition is anchored by a precision sandwich assembly comprising a 1/32-inch thick transparent acrylic clamping plate and a high-compliance silicone rubber cushion [2], [12]. This assembly is secured to the rigid adapter PCB using four lightweight M1.2 Phillips-head screws, facilitating a straightforward integration process with standard micro-tools. The clamping plate incorporates a precision-machined notch that serves a dual purpose: it guides the initial routing of the thin-film probe. It acts as a strategic folding point for strain relief, thereby preserving trace integrity during chronic recording. Concurrently, the silicone rubber layer serves as a conformal buffer, compensating for micro-scale surface irregularities and ensuring uniform contact pressure and intimate electrical engagement between the probe's electrode pads and the PCB contacts.

III. Circuit Implementation And Routing Strategy

A. Headstage Circuit Architecture and Signal Flow

The recording performance of the proposed mini-pedestal connector is enabled by a custom 256-channel headstage specifically optimized for high-density neural signal acquisition. As illustrated in Fig. 2, neural signals are processed through a hierarchical signal chain that preserves signal fidelity from the electrode–tissue interface to digitization.

The headstage integrates four Intan RHD2164 analog front-end (AFE) integrated circuits (ICs), designated as chips #1–#4. Each AFE incorporates a 64-channel low-noise amplifier array, 32:1 multiplexers, and on-chip 16-bit analog-to-digital converters (ADCs), collectively enabling simultaneous acquisition from 256 recording channels [13].

To accommodate the high aggregate data throughput at the system's nominal sampling rate of 20 kHz, the headstage architecture is partitioned into two 128-channel Serial Peripheral Interface (SPI) groups, designated Port I and Port II. Port I interfaces with chips #1 and #2, while Port II interfaces with chips #3 and #4. This parallelized communication scheme reduces SPI bus loading and ensures stable, high-speed data transfer without compromising timing margins.

Ensuring signal integrity across electrically noisy environments is a fundamental requirement for implantable recording platforms. To this end, low-voltage differential signaling (LVDS) is employed for critical communication pathways between the headstage and the controller. The use of differential signaling for chip select ($\overline{CS}$), serial clock (SCLK), and master-out–slave-in (MOSI) lines provide robust common-mode noise rejection while effectively decoupling high-speed digital switching from the sensitive microvolt-level analog front end [14]. Such a configuration ensures high-performance digital communication without compromising the noise floor of the neural signal acquisition system.

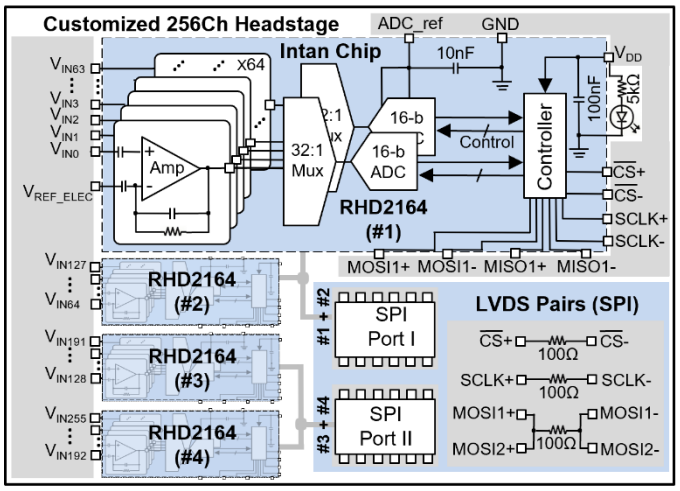

Fig. 2. Circuit architecture of the customized 256-channel headstage. Functional block diagram showcasing the hierarchical signal flow from the neural electrodes (256 channels) to the digital controller. The architecture integrates four RHD2164 analog front-end chips (#1 to #4), each featuring a 64-channel amplifier array, 32:1 multiplexers, and 16-bit ADCs. The front-end is organized into two independent 128-channel SPI groups (Port I and Port II).

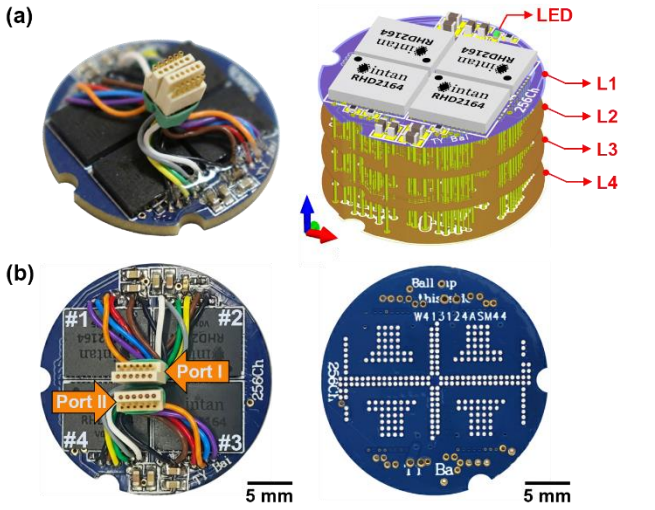

Fig. 3. Physical implementation and structural layout of the 256-channel headstage. (a) Photograph of the fully assembled 256-channel headstage (left) and its 3D structural layout (right), highlighting the integrated shielding and the stacked functional layers (L1–L4). (b) Detailed view of the PCB top side (left) showing the placement of four symmetrically arranged RHD2164 chips (#1 to #4) and Port I/II connectors, alongside the bottom side (right) featuring the high-density ball grid array (BGA) array for insertion-free elastomeric interfacing.

To mitigate transient current loads during simultaneous 16-bit ADC switching across the four RHD2164 chips, a localized decoupling strategy is employed. 10 nF and 100 nF bypass capacitors are positioned adjacent to the V_{DD} pins of each controller to minimize trace inductance and supply instantaneous high-frequency currents. This local decoupling is augmented by continuous internal power and ground planes within the four-layer stackup, which provide distributed inter-plane capacitance and low-impedance return paths. These measures suppress transient voltage drop and cross-band noise, facilitating stable signal acquisition across the analog front-end.

B. Headstage Layer Stack

The physical realization of the 256-channel headstage prioritizes extreme miniaturization without compromising signal quality. As shown in Fig. 3(a), the headstage is implemented on a high-density, four-layer PCB with a compact circular footprint of 25 mm in diameter. To ensure precise mechanical seating and facilitate hardware reuse, the PCB features two arc-shaped alignment notches. The headstage is keyed to the pedestal housing through these notches to prevent rotation during cap tightening. The arc-shaped profile was deliberately chosen over triangular notches to minimize surface wear and friction during repeated mating cycles.

The four-layer stackup (L1–L4, Fig. S1) is optimized to manage dense 256-channel routing within a 25-mm footprint while ensuring signal integrity. Layer 1 (top) hosts the analog front-end ICs and miniaturized passives. To minimize digital-to-analog crosstalk, critical high-speed SPI communication lines are buried within the inner layers: Layer 2 carries differential CS and SCLK pairs shielded by ground (GND) copper pours, while Layer 3 routes differential MOSI pairs and distributes Power (V_{DD}). Layer 4 (bottom) serves as a continuous GND plane to ensure stable signal return paths and accommodates the high-density BGA elastomeric interface.

On the top layer, the four RHD2164 chips are arranged in a symmetric configuration, with chips #1/#2 forming one pair and chips #3/#4 forming the second [Fig. 3(b)]. The reference (REF) pins of each chip pair are shorted and tied to a common system ground to ensure baseline consistency across the electrode array. To achieve high component density, the design employs ultra-miniaturized 0402-size surface-mount resistors and 0603-size capacitors. A green 0402 LED is integrated into the top layer as a real-time power indicator.

For data transmission, the system utilizes two 12-pin Omnetics A79621 connectors positioned at the center of the headstage. This central placement provides a significant mechanical advantage: as the threaded cap rotates during assembly, the wire bundles—organized and secured by heat-shrink tubing—pass directly through the circular aperture in the cap's center. This configuration ensures that the wires do not interfere with the mechanical housing or undergo twisting during rotation, effectively isolating the delicate interconnects from rotational torque.

Furthermore, the central connector placement facilitates a spatial star-grounding topology. To avoid the electromagnetic interference (EMI) loop antennas often cause when split analog/digital planes are used, the system utilizes a unified, continuous ground plane. This configuration promotes a compact return-current path near the connector region, reducing the likelihood of digital switching noise coupling into peripheral analog traces. Impressively, despite housing 256 channels and supporting electronics, the PCBs weigh merely 2.8 g. This ultra-lightweight profile substantially mitigates mechanical loading at the surgical site compared to conventional commercial systems.

C. Mechanical Interface Characterization and Interconnect Reliability

To evaluate the reliability of the proposed insertion-free mating system, we performed a comprehensive morphological and mechanical characterization of the anisotropic conductive elastomer interposer, as its material behavior fundamentally dictates the stability and repeatability of neural signal acquisition across the 256-channel interface. This component consists of a high-density array of conductive pillars embedded within a compliant elastomeric matrix, functioning as a microscale mechanical and electrical bridge between the headstage and the adapter PCB.

Morphological characterization, as depicted in Fig. 4, reveals a uniform hexagonal arrangement of conductive pillars characterized by an average diameter of 105 μm and a height of 385 μm. These vertically aligned microstructures establish independent conductive pathways between the ball grid array multichannel interconnections through surface contact while obviating the need for rigid, alignment-sensitive precision pins.

The interfacial compressive mechanics were investigated through correlated experimental observations and finite element analysis (FEA), with a specific focus on tolerance to pitch mismatch and misalignment. In the uncompressed state, the conductive pillars exert minimal contact force and exhibit negligible internal stress. Upon application of manual torque through the threaded cap—resulting in an initial elastomeric compression of 5%—the pillars establish firm seating against the PCB pads. At this stage, a uniform von Mises stress distribution develops across the contact regions, marking the initiation of stable electrical engagement.

Under increased axial compression (20% strain), the conductive pillars undergo controlled elastic deformation, which substantially expands the effective electrical contact area. FEA simulations corroborate that peak stress localizes primarily at the upper and lower contact interfaces of the pillars, while the elastomeric matrix ensures a uniform strain distribution across the array. This strategic stress localization promotes the formation of low-impedance conductive pathways while mitigating excessive mechanical loading that could compromise long-term interface reliability.

The robust alignment tolerance of the interconnect is achieved through a deliberate overprovisioning strategy, where the conductive pillar density significantly exceeds that of the PCB contact pads. This structural redundancy ensures that multiple pillars bridge each electrode-pad interface, thereby preserving stable electrical connectivity across all 256 channels even under moderate radial misalignment between the headstage and adapter PCBs. Together, these design features yield a compliant, alignment-tolerant interconnection architecture that supports reliable electrical connectivity in high-density chronic neural recording systems.

D. Adapter PCB Design and Routing Strategy

The adapter PCB (Fig. 5) serves as the foundational interface within the mini-pedestal, bridging the high-density connection from the polymer neural interface to the modular headstage. To

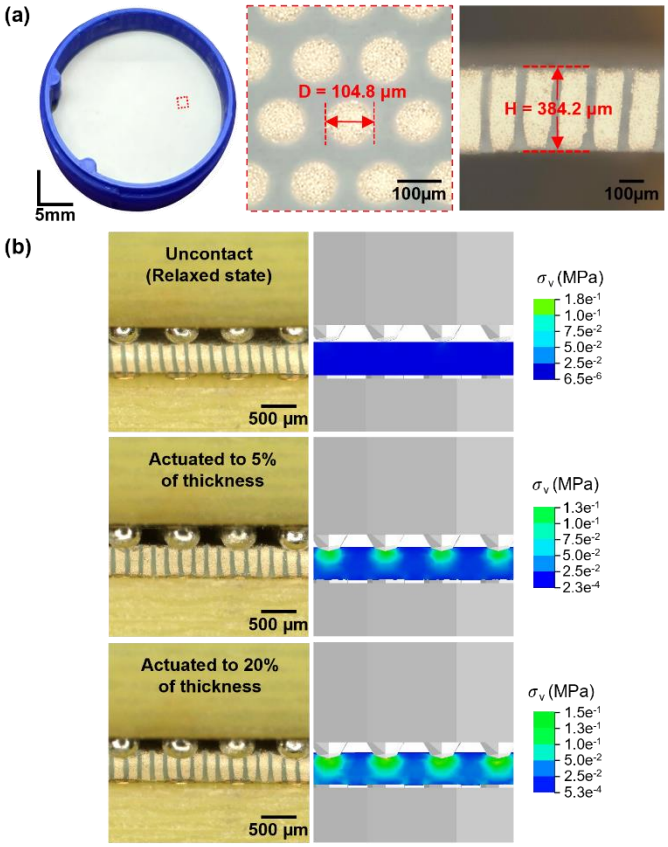

Fig. 4. Mechanical interface characterizations. (a) Morphological characterization of a conductive pillar-embedded elastomer sheet: microscopic analysis of the top-view distribution and cross-sectional profile. (b) Mechanical response and stress distribution of alignment-free conductive pillar interfaces with pitch mismatch: microscopic photographs and corresponding FEA stress simulations of the elastomer in the relaxed state, 5% compression, and 20% compression.

accommodate 256 independent signal channels within a confined circular area, we implemented a four-layer fan-out architecture with vertical blind vias that transit signals between layers while minimizing lateral routing space. This strategy enables a routing pitch significantly finer than standard through-hole or ball grid array configurations, which is essential for achieving the required channel density.

The top surface of the adapter PCB features a high-density pad array [Fig. 5(a), left] specifically optimized to interface with the conductive pillar-embedded elastomer. To maximize insertion-free contact reliability, no solder mask is applied to the top layer, allowing the gold-plated pads to remain elevated above the PCB surface. This protruding profile ensures intimate mechanical engagement and stable electrical contact with the conductive pillars under axial compression.

The bottom layer of the adapter PCB features a high-density BGA footprint [Fig. 5(a), right] optimized for direct coupling with the polymer neural interface, thereby facilitating a seamless, low-impedance signal transition from the electrodes to the backend electronics. Signals are distributed through the four-layer stackup using blind vias [Fig. 5(b)] for vertical interconnects, effectively managing crosstalk and maintaining signal fidelity across the full recording bandwidth. The entire

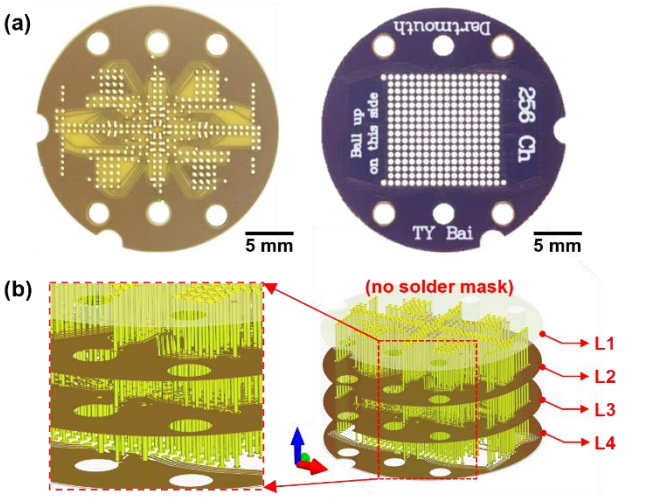

Fig. 5. Adapter PCB design and high-density routing strategy. (a) Optical photographs of the adapter PCB. The top side (left) features a 256-channel gold pad array designed without a solder mask on the top side of the first layer, allowing the gold-plated pads to remain extruded from the surface to facilitate intimate mechanical engagement with the elastomeric conductive pillars. The bottom side (right) features a high-density 256-channel BGA array for interface integration. (b) 3D exploded view illustrating the 4-layer fan-out architecture and the implementation of vertical interconnects using blind vias.

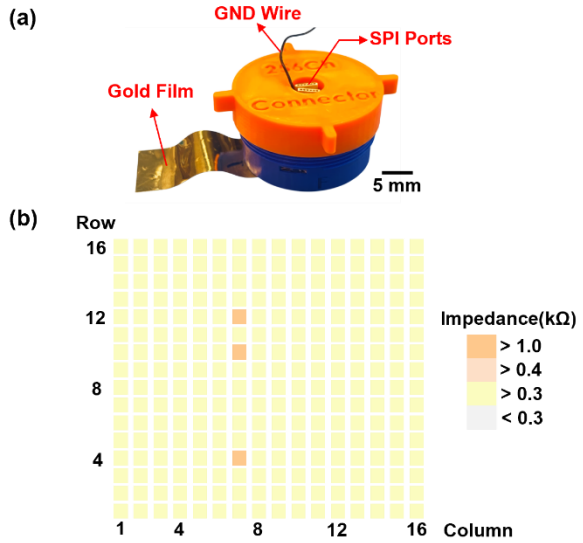

Fig. 6. Contact impedance characterization of the 256-channel interface. (a) Photograph of the mini-pedestal connector integrated with a gold film for contact validation. (b) 16×16 spatial heatmap illustrating the contact impedance distribution.

adapter assembly seats securely on an internal shoulder within the mini-pedestal housing, providing mechanical stability for the rotational compression mechanism.

Beyond spatial efficiency, this multi-layer routing architecture orchestrates a critical geometric remapping by translating the application-specific, often non-uniform fan-out patterns of the flexible probe into a standardized, symmetric pad matrix on the top layer. The design resolves the routing complexity inherent in converting irregular electrode footprints into a repeatable, high-density grid. This architectural transformation ensures that the 256-channel array is condensed into a compact, uniform layout suitable for elastomeric interfacing, while strictly adhering to manufacturing design rules for trace width and spacing clearances.

IV. Experimental Results And Characterization

A. Contact Impedance Characterization

To validate the electrical reliability of the 256-channel insertion-free interface, we performed spatial impedance mapping using a gold film test interface [Fig. 6(a)]. As illustrated in the 16 × 16 heatmap in Fig. 6(b), the system achieves remarkable uniformity across the high-density array.

The majority of channels demonstrate contact impedance within the range of 0.3-0.4 kΩ. This high degree of uniformity confirms that the threaded housing assembly, which converts manual torque into uniform axial pressure, successfully distributes the controlled load across the adapter PCB's entire 25-mm footprint. Three specific channels exhibited impedance exceeding 1.0 kΩ. These three channels were identified as non-functional due to inherent hardware defects originating from the high-density chip-to-PCB soldering process during headstage fabrication, specifically related to sub-optimal reflow of the 0.3-mm-pitch BGA pins, rather than failure of the mechanical connector interface itself.

B. FEA Validation

To provide a theoretical foundation for the observed electrical consistency, we conducted FEA to evaluate the mechanical behavior of the 256-channel interface under operational loads. The simulation specifically modeled the structural response during 20% thickness compression of the anisotropic conductive elastomer, corresponding to the typical displacement achieved by threaded manual assembly.

As shown in Fig. 7, the maximum principal strain (ε_{max}) on the upper BGA ball array is highly localized at the apex of each contact point. This strain concentration facilitates penetration of microscopic surface oxidation or contaminants on the gold-plated pads, thereby establishing stable, low-impedance electrical pathways. The simulation reveals that while local strain is sufficient for mechanical interlocking, overall stress remains well within the elastic limits of both the PCB substrate and the medical-grade encapsulation, ensuring that headstage components are not subjected to damaging mechanical deformation.

The stress distribution on the bottom pad array of the adapter PCB further validates the efficacy of the rotational-to-axial conversion strategy. Despite the manual nature of the tightening process, the threaded housing effectively translates torque into uniform pressure across the entire 25-mm footprint. This mechanical uniformity explains the high spatial consistency observed in the impedance heatmaps. By maintaining the conductive pillars under controlled axial compression, the system provides a robust, insertion-free interconnection that resists minor mechanical shocks and biological tissue shifts common in chronic neural recording applications.

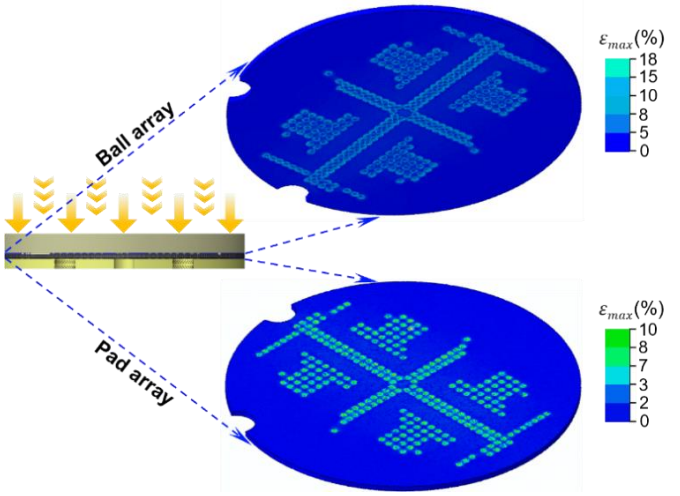

Fig. 7. FEA simulation of stress distribution at the upper and bottom contact interfaces. The simulation illustrates the localized maximum principal strain (ε_{max}) across the (a) upper ball array and (b) bottom pad array during the 20% thickness compression phase. The uniform stress distribution validates the mechanical efficacy of the threaded housing in providing stable electrical interlocking across all 256 channels.

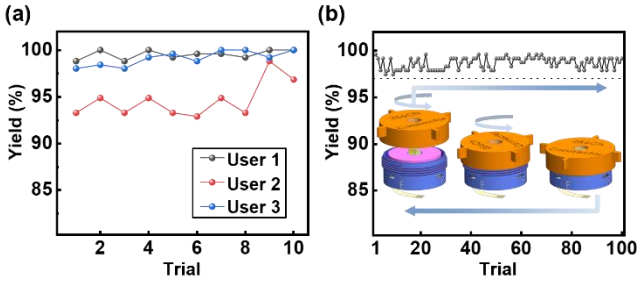

Fig. 8. Operational reproducibility and repeatability. (a) Connection yield across 10 assembly trials performed by three different users, demonstrating the robustness of the manual threaded interface against operator-induced variations. (b) Long-term stability analysis of the insertion-free interconnect, illustrating a maintained connection yield exceeding 97% across 100 consecutive mating trials.

C. Operational Reliability and Reproducibility

A critical requirement for chronic neural interfaces is consistent performance regardless of operator or number of use cycles. To evaluate the human-factor reproducibility of our design, we conducted ten assembly trials performed by three independent users. The results, summarized in Fig. 8(a), reveal that connection yield remained high and consistent across all operators. This demonstrates that the manual threaded assembly effectively standardizes the axial pressure required for interlocking, decoupling electrical performance from the specific torque or technique applied by different users.

We investigated the long-term structural robustness and evaluated the material's compression set of the insertion-free interface through a mixed-mode longitudinal durability test. To simulate a chronic experimental lifecycle, the system underwent 100 mating trials distributed over five days (20 manual cycles per day). Between testing sessions, the assembly was continuously maintained in its fully mated, 20% statically compressed state. As illustrated in Fig. 8(b), the connection yield remained exceptionally stable, consistently exceeding 97%. This high repeatability is attributed to the solder-mask-free design of the adapter PCB and the compliant nature of the conductive elastomer, which together prevent permanent mechanical deformation of the contact pads even after extensive cycling.

To evaluate resilience under dynamic in vivo conditions, the assembled mini-pedestal underwent extended mechanical vibration testing (120 minutes) with acceleration profiles ranging from normal locomotion (8.0 m/s²) to extreme physical stress (22.9 m/s²). The system demonstrated excellent mechanical stability, maintaining a connection yield of 98.8% with negligible contact-impedance drift (Fig. S2).

Furthermore, environmental sealing was verified through a prolonged exposure test, with the active thin-film probe fully immersed in a phosphate-buffered saline (PBS) bath for three days. Subsequent disassembly confirmed that the internal elastomeric interface and adapter PCB remained completely dry, demonstrating that the physical barrier provided by the threaded cap, foam washer, and potting compound effectively prevents fluid ingress and ensures operational stability in fluidic environments.

D. Thermal Stability and Heat Dissipation Analysis

Effective heat regulation within high-density neural interfaces remains critical for preventing localized tissue damage and ensuring the operational longevity of onboard electronics. Characterization of the 256-channel mini-pedestal connector's thermal behavior occurred during continuous high-speed data acquisition. As illustrated in Fig. 9, real-time temperature monitoring spanned a 4-hour period, simulating an intensive recording session under full-bandwidth SPI operation.

To evaluate the system's thermal safety under peak operational load, we characterized its performance during continuous 256-channel data acquisition at a high sampling rate of 20 kHz. Real-time temperature monitoring in a PBS bath shows that the housing temperature increases gradually after data acquisition begins, reaching a steady-state value of approximately 30.5 °C after 35 minutes. The absolute operating temperature remains significantly lower than the typical biological baseline (37 °C). More importantly, the localized temperature elevation is maintained well within the stringent physiological safety limit of < 2 °C, ensuring that the assembly's modular structural architecture effectively dissipates the heat generated by the four RHD2164 chips [15]. By preventing heat accumulation during intensive recording sessions, the design ensures the long-term integrity of the electrode–tissue interface and the functional stability of the onboard electronics, fulfilling a critical requirement for high-density, chronic neural interfaces.

The infrared thermography inset in Fig. 9 provides detailed spatial mapping of the system's thermal dissipation characteristics at steady state. The results indicate that thermal energy is distributed uniformly across the headstage architecture and efficiently dissipated through the mini-pedestal

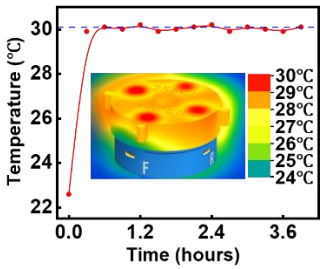

Fig. 9. Thermal stability characterization of the 256-channel connector during continuous operation. Real-time temperature monitoring conducted over a 4-hour duration under continuous full-bandwidth SPI data transmission at the 20 kHz maximum sampling rate. Inset: Infrared thermography illustrating the spatial temperature distribution across the headstage and mini-pedestal assembly at steady state, highlighting the efficient heat dissipation of the modular architecture.

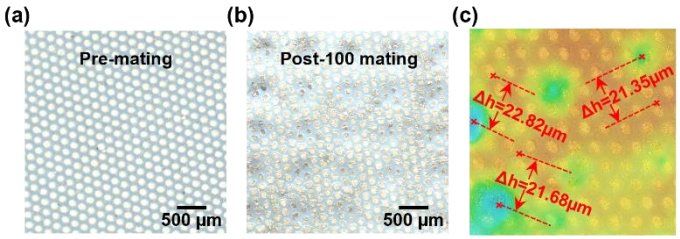

Fig. 10. Mechanical durability and surface topography analysis of the elastomeric interposer. (a) Optical micrograph showing the surface morphology of the interposer in its pre-mating (pristine) state. (b) Post-mating inspection after 100 consecutive mating cycles, demonstrating high structural integrity and minimal mechanical wear of the conductive pillars. (c) 3D surface topography mapping and corresponding recessed depth variations (Δh) across the array, validating the uniformity of the mechanical interface.

housing. Efficient heat dissipation prevents the formation of localized thermal hotspots, safeguarding both the structural integrity of the polymer neural interface and the underlying biological tissue from adverse thermomechanical stress.

Synergizing this thermal resilience with the mechanical stability of the insertion-free elastomeric interconnect guarantees sustained, high-fidelity signal acquisition over chronic implantation periods. The system maintains this high performance without relying on active cooling or restrictive duty cycles, facilitating continuous, high-bandwidth neural recording in freely behaving models.

E. Mechanical Durability

The long-term operational reliability of the 256-channel mini-pedestal connector is fundamentally governed by the mechanical resilience of the insertion-free elastomeric interface, particularly its capability to maintain structural integrity under repetitive mating-induced strain. To investigate the potential for material fatigue or permanent pillar deformation, we subjected the assembly to a 100-cycle durability protocol to simulate the extended lifecycle requirements of a modular neural headstage. This evaluation was complemented by high-resolution characterization of the interposer's surface topography, enabling a detailed comparative analysis of the microstructures in both pre- and post-cycling states to validate long-term mechanical stability.

As illustrated in Fig. 10(a), the pristine interposer exhibits a highly uniform surface morphology with well-defined conductive pillars. Following 100 consecutive mating and unmating cycles simulating intensive longitudinal use, microscopic inspection in Fig. 10(b) revealed that the interposer maintained its morphological integrity with negligible surface degradation or pillar deformation. Although minor dark residues are visible in the post-cycling micrographs, these were identified as trace metallic debris transferred from the headstage solder balls during repeated axial compression. This exogenous particulate matter did not compromise the elastomeric structure or the electrical conductivity of the interface, confirming the interposer's robust resistance to mechanical wear.

Quantitative 3D surface mapping Fig. 10(c) was utilized to assess the structural fidelity of the recessed interface, providing a high-resolution profile of the mechanical engagement across the array. Measurements yielded highly consistent recess depths with representative values of 22.82 µm, 21.35 µm, and 21.68 µm, demonstrating that the axial load is distributed with sub-micron precision across the 25-mm footprint. This minimal spatial variance confirms that the elastomeric interposer facilitates stable and uniform contact force, which is a prerequisite for ensuring low-impedance electrical coupling in high-density neural implants. Such mechanical robustness ensures that signal quality remains uncompromised over the device's operational lifespan, thereby fulfilling a critical engineering requirement for the chronic stability and signal integrity of high-bandwidth neural recording platforms.

F. In Vitro Electrical Characterization

Evaluation of the 256-channel interface's electrical integrity was conducted via comprehensive impedance spectroscopy utilizing a high-density polyimide-based ECoG array. This array architecture, which occupies a 400 × 400 µm² active area, features 60 × 60 µm² gold electrodes optimized for high-resolution neural recording.

Spatial electrode impedance mapping was conducted at 1 kHz to evaluate contact consistency across the large-scale insertion-free interface. As shown in the color-coded heatmap in Fig. 11(a), the system achieved exceptional uniformity across all 256 channels. Statistical analysis reveals that impedance magnitudes follow a tight Gaussian distribution with a mean of 397 kΩ and a standard deviation (SD) of 38.2 kΩ.

Benchmarking of the acquisition fidelity involved a rigorous comparative characterization between the custom 256-channel headstage and a commercial Intan reference system. The resulting distributions, presented in Fig. 11(b), show the two platforms exhibit nearly identical profiles, with the Intan-benchmarked data yielding a mean impedance of 395 kΩ and an SD of 37.8 kΩ. This high degree of spectral overlap confirms that the elastomeric-based interconnect facilitates a reliable and repeatable electrical coupling that is functionally indistinguishable from established industrial hardware, ensuring transparent signal transmission regardless of the hardware configuration.

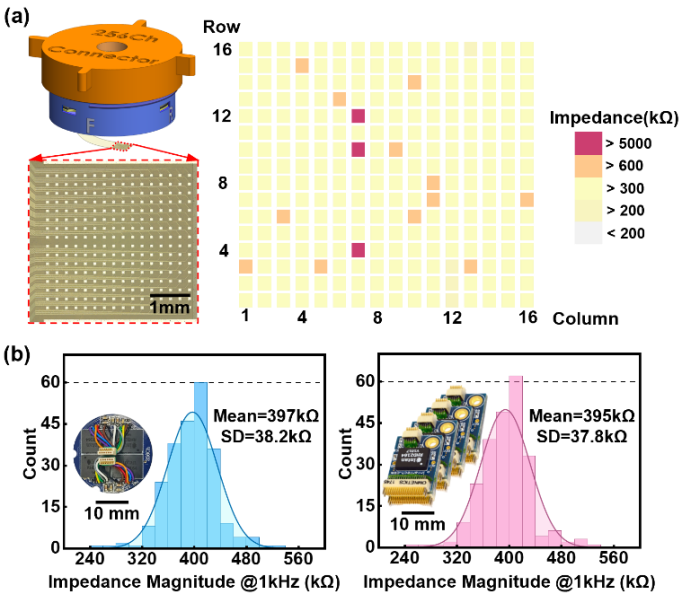

Fig. 11. Electrical characterization and impedance mapping of the 256-channel ECoG array. (a) Spatial electrode impedance mapping across the 400×400 μm^2 active area, featuring 60×60 μm^2 gold electrodes. The color-coded heatmap confirms exceptional contact uniformity and signal integrity across the entire 256-channel, insertion-free interface. (b) Comparative impedance distribution at 1 kHz benchmarked against a commercial Intan headstage to ensure hardware reproducibility. The experimental data are overlaid with Gaussian fit curves (solid lines), highlighting the tight impedance distribution. The high degree of spectral overlap confirms that the customized system achieves electrical coupling performance that is functionally equivalent to that of established commercial data-acquisition hardware.

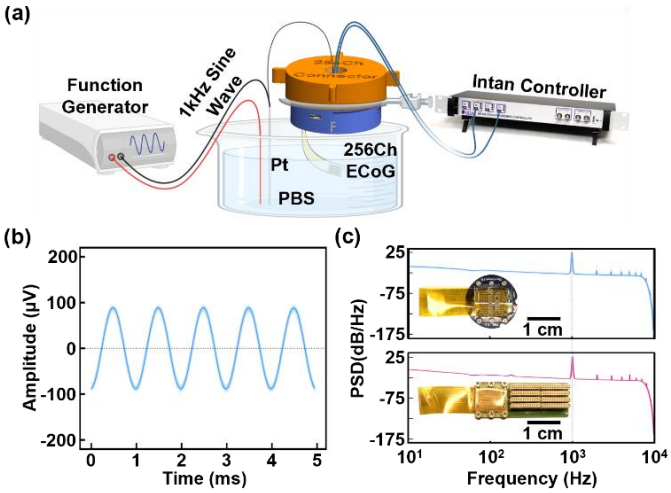

Fig. 12. Dynamic signal acquisition fidelity and frequency response validation via sine wave benchmarking. (a) Schematic of the in vitro test configuration in a PBS bath to emulate physiological loading conditions. (b) Simultaneously recorded 1 kHz sinusoidal waveforms from all 256 channels; the consistent overlay and the ensemble average (thick blue line) demonstrate high spatial uniformity and undistorted capture. (c) Comparative power spectral density (PSD) analysis between the customized system (blue) and the commercial Intan reference (pink). The identical signal peaks and overlapping noise floors across the full bandwidth (10 Hz – 10 kHz) validate that the proposed architecture preserves signal fidelity without introducing significant parasitic interference.

G. Signal Fidelity and Noise Floor Characterization

To evaluate the dynamic signal acquisition performance of the 256-channel integrated system, we conducted in vitro validation using a 1-kHz sinusoidal input (approximately 20 mV peak-to-peak) in a PBS bath to emulate physiological loading conditions, as illustrated in Fig. 12(a).

The recorded waveforms across the entire 256 channels, shown in Fig. 12(b), exhibit clean, undistorted capture of the 1-kHz signal, with no observable phase offset or inter-channel amplitude variation. The ensemble average across all channels, represented by the thick blue trace, further confirms the exceptional spatial uniformity enabled by the insertion-free mini-pedestal architecture. It is noted that the absolute signal amplitude is attenuated relative to the applied excitation due to the impedance of the electrode–electrolyte interface and the AC-coupled front-end; however, this attenuation is global and consistent across channels and therefore does not affect the assessment of interconnect integrity or channel-to-channel uniformity.

To further quantify acquisition fidelity, we performed a power spectral density (PSD) analysis over a 10 Hz to 10 kHz bandwidth. As shown in Fig. 12(c), the spectral profile of our custom headstage (blue trace) is benchmarked against a commercial Intan headstage system (pink trace). Both systems exhibit a dominant 1-kHz signal peak corresponding to the input frequency, accompanied by well-defined higher-order harmonics (2f, 3f, ...) that indicate excellent linearity in the signal chain.

Achieving a minimal intrinsic noise floor is a fundamental prerequisite for high-fidelity neural recording, particularly for accurately capturing low-amplitude signals such as local field potentials (LFPs) and single-unit action potentials. Evaluation of the electronic noise performance across the 256-channel mini-pedestal system involved shorting all input channels through a gold-film interface, a methodology that effectively isolates noise contributions from the custom PCB routing and connector assembly from the intrinsic noise of the active electronics [5], [16]. These characterizations were conducted across a frequency bandwidth of 0.1 Hz to 7.5 kHz, a range intentionally matched to the standard operational configuration and on-chip low-pass filter cutoff of the Intan RHD2164 controller.

The statistical distribution of the root-mean-square (RMS) noise across the full 256-channel array is presented in Fig. 13(a), revealing a tight Gaussian profile with a mean of 2.68 μV and a standard deviation (SD) of 0.46 μV. This empirical performance closely approximates the theoretical noise limit of 2.4 μV specified for the Intan RHD2164 chips [17]. Such precise alignment between the measured data and theoretical specifications demonstrates that the custom four-layer PCB stackup effectively suppresses EMI and mitigates digital-to-analog crosstalk by utilizing internal ground planes and strategic trace separation. This robust noise performance ensures that the system maintains high signal-to-noise ratios (SNR) even when deployed in electromagnetically active research or clinical settings.

Spectral analysis using PSD revealed the system's noise characteristics across the operational bandwidth, as illustrated

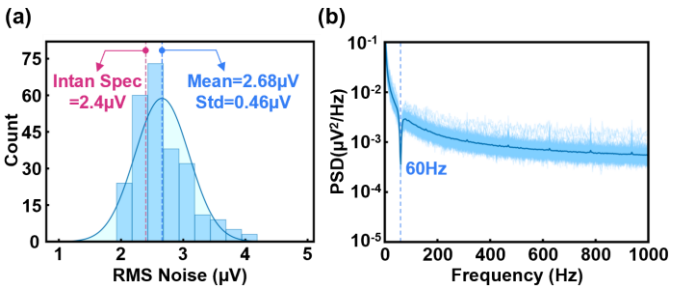

Fig. 13. System noise characterization with shorted input channels for sensitivity validation. (a) Statistical distribution of the RMS noise across all 256 channels; the experimental data (blue bars) are overlaid with a Gaussian fit (solid curve), yielding a mean value of 2.68 μV. This measured performance closely matches the theoretical amplifier limit, validating the effectiveness of the custom circuit design and shielding. (b) Power spectral density (PSD) analysis reveals a clean, broadband noise across the physiological frequency range, with the primary interference limited to the characteristic 60 Hz line-frequency peak.

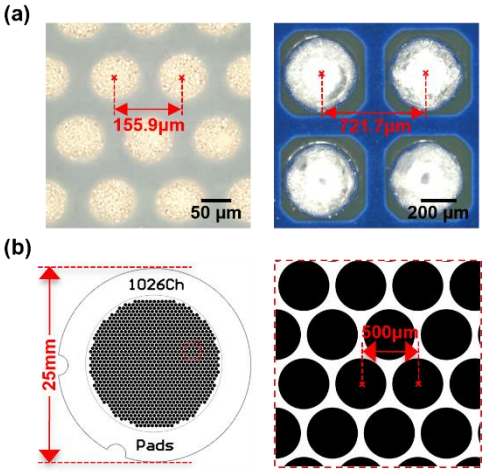

Fig. 14. Scalability analysis and technical roadmap toward 1024-channel high-density integration. (a) Comparative footprint analysis between the fine-pitch elastomeric conductive pillars and standard industrial solder balls, highlighting the superior packaging density afforded by the insertion-free interconnect strategy. (b) Conceptual pathway for scaling the mini-pedestal connector from 256 to 1024 channels within the same 25 mm diameter footprint for ultra-high-density polymer neural interfaces.

in Fig. 13(b). Within the primary neural recording range of 10 Hz to 10 kHz, the architecture exhibits a notably clean, flat broadband noise floor that is largely consistent with the commercial Intan reference across the entire spectrum. This spectral flatness indicates that the system noise is dominated by the thermal noise of the input stage, suggesting that no significant 1/f noise or parasitic oscillations were introduced by the insertion-free interconnect. Additionally, the frequency response exhibits sharp attenuation at a cutoff frequency of 7.5 kHz, a characteristic that aligns precisely with the integrated low-pass filter settings of the RHD2164 amplifier.

Environmental interference is primarily confined to a localized peak at 60 Hz and its subsequent harmonics, which represent standard power-line noise and are readily addressed through digital notch filtering during post-processing. The observed spectral consistency across the recording bandwidth demonstrates that the custom hardware maintains signal integrity comparable to that of established high-bandwidth neural recording systems. Validation of this insertion-free mini-pedestal architecture confirms its utility as a high-SNR solution that supports the data acquisition requirements of long-term electrophysiological research. By ensuring a high raw data fidelity, this interface provides the precision needed for accurate feature extraction and robust on-device processing, thereby supporting reliable performance in large-scale neural monitoring and real-time BCIs research paradigms. Furthermore, the high-density scalability and mechanical robustness of this platform suggest significant potential for translation into next-generation clinical neural interface [18].

V. Discussion

A. Scalability Analysis: Pathway to 1024 Channels

The inherent scalability of anisotropic elastomeric technology represents a transformative shift from traditional rigid interconnects, offering a viable roadmap for the next generation of massive-scale neural interfaces. Evaluation of the spatial efficiency in Fig. 14(a) highlights a significant geometric advantage, where the fine-pitch conductive pillars (156 μm pitch) provide a 3.2× reduction in interconnect pitch compared to standard solder-ball arrays. This dimensional miniaturization is facilitated by eliminating bulky plastic housings and individual pin-and-socket architectures, allowing contact density to be governed primarily by PCB fabrication resolution and the elastomer's pillar frequency.

Analysis of the current mini-pedestal footprint suggests that the system can accommodate a 1024-channel high-density array within the same 25-mm-diameter envelope. This integration pathway, conceptualized in Fig. 14(b), relies on optimizing the four-layer PCB fan-out and refining the pillar arrangement to increase channel density without necessitating significant modifications to the existing mechanical compression housing. Such an expansion would involve migrating to a high-density interconnect (HDI) PCB process with finer trace/space design rules, effectively quadrupling the recording bandwidth while maintaining the lightweight, low-profile advantages of the current architecture.

B. Substrate Compatibility and Generalizability

A key advantage of the E-Link architecture is the mechanical decoupling of the mating interface from the functional substrate. While FEA indicates localized von Mises stress at the interposer during 20% axial compression, this load is entirely absorbed by the rigid adapter PCB and its supporting internal pedestal step. Because the thin-film probe is anchored to the underside of the adapter PCB, it remains outside the primary load path and experiences zero mating-induced strain. This structural isolation ensures that the system is not limited to stiff substrates like polyimide, but can safely accommodate ultra-low-modulus materials, such as hydrogels or soft silicones, without risking trace deformation or plastic fracture.

The sandwich assembly employs a modular design to

accommodate diverse substrate materials and thicknesses. The 1/32-inch transparent acrylic plate serves as a universal rigid backing, its thickness determined by the mini-pedestal's internal mechanical clearance. In contrast, the high-compliance silicone cushion serves as the primary tunable variable. For substrates significantly thicker or softer than standard polyimide (e.g., hydrogels), the cushion's thickness and durometer—controllable via spin-coating speed—are adjusted to match the probe's volumetric profile conformally. This tunable compliance prevents localized 'pinching' or trace deformation, ensuring uniform contact pressure and reliable electrical engagement across varying material platforms.

C. Comparison with State-of-the-Art Performance

Comparative assessment of the 256-channel mini-pedestal connector against established research and commercial headstages, as summarized in Table I, highlights significant performance breakthroughs in both channel density and mass. Quantitative analysis reveals that the proposed architecture achieves a substantial leap in channel count while maintaining a remarkably lightweight form factor of 2.8 g. This weight optimization proves particularly vital for longitudinal studies in small animal models, where minimizing head-mounted loads remains essential for preserving naturalistic behaviors and reducing localized mechanical strain at the implant site. Achieving such a high density-to-weight ratio ensures that the device remains a transparent interface for the subject, facilitating high-fidelity data acquisition without interfering with the biological phenomena under observation.

Superior scalability further distinguishes this design from commercial Intan-based headstages, which are frequently constrained to 64 or 128 channels within a comparable physical footprint. The mini-pedestal architecture establishes a validated framework for 256-channel acquisition while maintaining a clear developmental trajectory toward 1024-channel integration. This methodology enables a fourfold increase in recording bandwidth without necessitating an expansion of the volumetric footprint, effectively addressing the growing demand for massive-scale neural data acquisition. This roadmap toward thousands of channels is enabled by the inherent pitch scalability of the anisotropic elastomer, which allows significantly finer contact spacing than conventional mechanical pins.

Beyond the electrical and density advantages, the integrated mini-pedestal housing serves as a robust mechanical shield that significantly enhances the thin-film probe's physical durability. This structural enclosure provides a protective barrier that isolates the delicate, flexible traces from environmental contaminants and accidental mechanical impacts during the movements of freely behaving subjects [19]. By serving as a rigid, standardized strain-relief platform, the housing effectively redistributes mechanical loads away from the sensitive electrode-to-PCB transition zone, thereby ensuring the overall longevity of the neural interface throughout chronic recording. This dual-purpose design, providing both high-density interconnection and structural shielding, represents a critical advancement in the engineering of reliable, long-term neural implants.

D. Implications for Neuroscience and IoMT

This streamlined, rotate-and-play architecture addresses the practical challenges of deploying high-density interfaces in demanding environments. By replacing error-prone procedures with a reliable one-step connection, the system reduces surgical handling time and interface damage, allowing researchers to focus entirely on neural data acquisition.

A critical requirement for chronic neuroscience studies is reliable neural recording in freely moving animals [20]. To address this need, the mini-pedestal features a circular, low-profile form factor that ensures direct compatibility with both mechanical and motorized commutators while maintaining an overall stack height that preserves the intended experimental fit. Mechanical stability under torque and dynamic motion associated with animal behavior is achieved through a compact, thread-based rotational-to-axial compression mechanism. This design minimizes the risk of intermittent contact, signal dropout, or mechanical failure. Collectively, these design considerations support robust deployment of the 256-channel interface in freely moving neuroscience experiments, where cable management constraints or rigid connector architectures can otherwise limit recording duration or behavioral complexity.

Standardizing high-density interfaces via this insertion-free methodology reduces technical barriers by eliminating the need for specialized micro-soldering and precision alignment. This empowers diverse laboratories to conduct large-scale recordings with high experimental reproducibility [21]. While currently targeting research applications, these core principles of mechanical compliance and scalable integration align directly with the operational requirements of Internet of Medical Things (IoMT) ecosystems, where device maintainability and deployment scalability represent critical design considerations [22].

E. Limitations and Future Directions

Transitioning from 256 to 1024 channels, as conceptualized in Fig. 14, represents a significant engineering leap that necessitates a thorough re-evaluation of data throughput and thermal dissipation strategies. While the 256-channel configuration strictly maintains physiological thermal safety, the increased power density of a 1024-channel array will necessitate active power management. This may involve integrating ultra-low-power application-specific integrated circuits (ASICs), dynamic voltage scaling, and advanced thermal interface materials to mitigate localized heating within the compact housing.

Future work will also prioritize integrating high-bandwidth wireless modules for untethered monitoring, alongside on-device processing frameworks to manage massive data streams. Finally, chronic in-vivo validation in freely behaving subjects remains essential to ensure long-term biocompatibility and signal stability across diverse environments.

TABLE I
COMPARISON OF COMMERCIAL AND RESEARCH HEADSTAGE

Publication	**2010** [23]	**2015** [24]	**2016** [7]	**2017** [25]	**2020** [26]	**2021** [27]	**2024** [28]	**2024** [29]	**2025** [30]	**2025** [10]	**This Work**
Channel #	128	128	256	128	128	256	64	128	128	128	**256**
Size (mm)	25.5 × 17.9 × 11	35 × 21 × 4	32 × 30 × 3	24 × 22 × 5	21 × 12 × 10	35.4 × 24.9 × 18	∅18.6 × 4	13.2 × 11.4 × 7	11 × 8 × 6	30 × 24 × 11	∅25 × 11
Weight (g)*	9.9 (Housed)	2.1 (PCB)	1.2 (PCB)	3.3 (PCB)	1.8 (PCB)	26.4 (Housed)	1.5 (PCB)	1.6 (Housed)	2.3 (PCB)	4.5 (PCB)	**2.8 (PCB) 6.6 (Housed)**
Electrode Interface[a]	Hirose DF30	Molex SlimStack	H&S ACF Film	Hirose ZIF	Samtec ADM6	LGA Stacking	Hirose DF40	Panasonic S35	Molex SlimStack	Samtec SEAF	**Elastomeric**
Mating Mechanics[b]	Rigid Plug	Rigid Plug	Permanent Bond	Rigid Plug	Rigid Plug	Compliant Compression	Rigid Plug	Rigid Plug	Rigid Plug	Rigid Plug	**Compliant Compression**
Data Interface[c]	Omnetics (12-pin)	Omnetics (12-pin)	LVDS (16-cable)	Omnetics (4-pin)	Omnetics (12-pin)	μHDMI	Omnetics (12-pin)	μHDMI	Omnetics (12-pin)	Tethered Board	**Omnetics (12-pin)**

* Weights are reported as specified in cited sources; the presence of protective housing varies among the developers.
[a] Connection method used for the Electrode interface board (EIB) or adaptor board.
[b] Rigid Plug: requiring high insertion force and precise alignment; Permanent Bond: disposable headstage; Compliant Compression: low-force mating, self-aligned.
[c] Interface to the data acquisition system.

VI. CONCLUSION

This work introduces a modular 256-channel mini-pedestal connector architecture that redefines the interconnection paradigm for chronic high-density neural interfaces. Utilization of an insertion-free elastomeric interposer, featuring alignment-tolerant conductive pillars and a mechanically compliant compression mechanism, facilitates a robust coupling solution that circumvents the insertion forces, alignment sensitivities, and mechanical fragilities inherent to traditional rigid pin-based systems. By transitioning away from permanent solder joints and rigid pins, the proposed design establishes a reliable electrical environment that prioritizes both structural longevity and ease of operation in complex surgical settings.

Empirical characterizations validate the system's high signal fidelity, reliable mechanical durability over repeated mating cycles, and strict adherence to physiological thermal safety limits. The integration of a lightweight form factor and a detachable architecture minimize the chronic head-mounted mass compared to conventional hardware, thereby mitigating behavioral artifacts and reducing localized tissue strain in freely behaving subjects. Implementation of this "rotate-and-play" insertion-free interface democratizes access to high-density neural recording by removing the requirement for specialized micro soldering expertise, effectively lowering the technical threshold for adoption in diverse neuroscience research environments. This user-centric approach ensures that the sophisticated capabilities of the system remain accessible for rapid deployment and cross-laboratory collaboration.

Scalability analysis indicates a clear developmental roadmap toward 1024-channel integration within the existing 25-mm footprint, leveraging the superior pitch density of elastomeric conductive pillars (156 μm pitch) compared to traditional solder ball or pin-based arrays. This expansion capability, combined with the architecture's potential for wireless module integration, positions the mini-pedestal connector as a highly versatile platform for next-generation BCIs and the expanding IoMT. Such scalability ensures that the hardware can evolve in tandem with the increasing demands of massive-scale neural data acquisition.

The fundamental design principles established in this study offer a versatile framework for bridging the gap between soft sensors and rigid electronics. By utilizing mechanical flexibility for alignment, ensuring even pressure through threaded components, and enabling reusability via insertion-free contacts, this approach addresses the persistent challenges of high-density bioelectronic interfacing. As neural technologies continue to scale to thousands of channels, the development of robust, scalable packaging becomes just as vital as the innovation of the sensors themselves. These combined strategies provide a repeatable and reliable method for connecting delicate neural probes to standardized hardware, effectively solving the "soft-to-hard" integration problem that has long hindered the deployment of large-scale implants.

ACKNOWLEDGMENT

The authors gratefully acknowledge support from NIH R01MH139342 and the Dartmouth PhD Innovation Fellowship.

REFERENCES

[1] P. Konrad, *et al.*, "First-in-human experience performing high-resolution cortical mapping using a novel microelectrode array containing 1024 electrodes," *J Neural Eng*, vol. 22, no. 2, Mar. 2025.
[2] Y. Qiang, *et al.*, "Monolithic three-dimensional neural probes from deterministic rolling of soft electronics," *Nat Electron*, vol. 8, no. 8, pp. 721-737, Aug. 2025.
[3] Y. Qi, *et al.*, "Stabilized carbon coating on microelectrodes for scalable and interoperable neurotransmitter sensing," *Nat Commun*, vol. 16, no. 1, pp. 3300, Apr. 2025.
[4] F. A. G. Mourao, *et al.*, "A Fully Adapted Headstage With Custom Electrode Arrays Designed for Electrophysiological Experiments," *Front Neurosci*, vol. 15, no. pp. 691788, 2021.
[5] T. Kaiju, M. Inoue, M. Hirata, and T. Suzuki, "Compact and low-power wireless headstage for electrocorticography recording of freely moving primates in a home cage," *Front Neurosci*, vol. 19, no. pp. 1491844, 2025.
[6] X. Zhang, et al., "Compact packaging of high-throughput flexible neural multielectrode arrays for in vivo recording," *Sens Actuators A Phys*, vol. 399, pp. 117347, Jan. 2026.
[7] G. Rios, E. V. Lubenov, D. Chi, M. L. Roukes, and A. G. Siapas, "Nanofabricated Neural Probes for Dense 3-D Recordings of Brain Activity," *Nano Lett*, vol. 16, no. 11, pp. 6857-6862, Nov. 2016.
[8] S. Y. Park, *et al.*, "A Miniaturized 256-Channel Neural Recording Interface With Area-Efficient Hybrid Integration of Flexible Probes and CMOS

Integrated Circuits," *IEEE Trans Biomed Eng*, vol. 69, no. 1, pp. 334-346, Jan. 2022.

[9] L. Wang, *et al.*, "High-density implantable neural electrodes and chips for massive neural recordings," *Brain-X*, vol. 2, no. 2, 2024.

[10] E. K. Jacobs, M. Monge, A. Switalla, R. A. Frederick, and F. Deku, "Iris 128x: open-source 128 channel headstages for neural stimulation and recording," *J Neural Eng*, vol. 22, no. 6, Nov. 2025.

[11] D. Yi, *et al.*, "3D Printed Skull Cap and Benchtop Fabricated Microwire-Based Microelectrode Array for Custom Rat Brain Recordings," *Bioengineering (Basel)*, vol. 9, no. 10, Oct. 2022.

[12] J. Ryu, *et al.*, "Multifunctional Nanomesh Enables Cellular-Resolution, Elastic Neuroelectronics," *Adv Mater*, vol. 36, no. 36, pp. 141, Sep. 2024.

[13] T. B. Yasar, *et al.*, "Months-long tracking of neuronal ensembles spanning multiple brain areas with Ultra-Flexible Tentacle Electrodes," *Nat Commun*, vol. 15, no. 1, pp. 4822, Jun. 2024.

[14] Q. Li, Z. Zhang, M. Shi, and X. Tao, "Multi-channel Neural Signal Recording System for an Implantable Brain-Computer Interface," *Annu Int Conf IEEE Eng Med Biol Soc*, vol. 2024, no. pp. 1-5, Jul. 2024.

[15] M. Rizk, *et al.*, "A fully implantable 96-channel neural data acquisition system," *J Neural Eng*, vol. 6, no. 2, pp. 026002, Apr. 2009.

[16] K. Barth, C. Schmitz, T. Jochum, and J. Viventi, "Intan Technologies integrated circuits can produce analog-to-digital conversion artifacts that affect neural signal acquisition," *J Neural Eng*, vol. 21, no. 4, Jul. 2024.

[17] Intan Technologies, LLC. (2021, Dec. 1). *RHD2164 Chip*. [Datasheet]. Available: https://intantech.com/files/Intan_RHD2164_datasheet.pdf

[18] C. H. Chiang, *et al.*, "Flexible, high-resolution thin-film electrodes for human and animal neural research," *J Neural Eng*, vol. 18, no. 4, Jun. 2021.

[19] M. Voroslakos, P. C. Petersen, B. Voroslakos, and G. Buzsaki, "Metal microdrive and head cap system for silicon probe recovery in freely moving rodent," *Elife*, vol. 10, May. 2021.

[20] J. P. Newman, *et al.*, "ONIX: a unified open-source platform for multimodal neural recording and perturbation during naturalistic behavior," *Nat Methods*, vol. 22, no. 1, pp. 187-192, Jan. 2025.

[21] J. H. Siegle, G. J. Hale, J. P. Newman, and J. Voigts, "Neural ensemble communities: open-source approaches to hardware for large-scale electrophysiology," *Curr Opin Neurobiol*, vol. 32, no. pp. 53-9, Jun. 2015.

[22] J. Y. Park, *et al.*, "Lessons Learned and Challenges Ahead in the Translation of Implantable Microscale Sensors and Actuators," *Annu Rev Biomed Eng*, vol. 27, no. 1, pp. 211-233, May. 2025.

[23] T.-D. Technologies. (2024). ZC128: ZIF-Clip Analog Headstages Technical Specifications. [Online]. Available: https://tdt.com/docs/hardware/zif-clip-analog-headstages/#zif-clip-zc-headstages-technical-specifications (Accessed: Jan. 29, 2026).

[24] Intan Technologies, LLC. (2025). *RHD2000_128-Channel Headstage*. [Datasheet]. Available: https://intantech.com/files/Intan_RHD2000_128_channel_headstage.pdf

[25] Neuropixels. (2024). 128Ch NRIC Datasheet. [Online]. Available: https://1d1204a4-e092-4bd5-ab7d-6d350a74299f.filesusr.com/ugd/328966_c59e77054175456cb0c3ef82b32219c1.pdf (Accessed: Jan. 29, 2026).

[26] Plexon. (2020.). Digital Headstage Technical Guide. [Online]. Available: https://plexon.com/wp-content/uploads/2020/01/Digital-Headstage-Technical-Guide.pdf (Accessed: Jan. 29, 2026)

[27] Blackrock Neurotech. (2024). CerePlex E256 Digital Headstage. [Online]. Available: https://blackrockneurotech.com/products/cereplex-e256/ (Accessed: Jan. 29, 2026).

[28] Open Ephys. (2024). Headstage-64: ONIX Hardware Guide. [Online]. Available: https://open-ephys.github.io/onix-docs/Hardware%20Guide/Headstages/headstage-64/index.html (Accessed: Jan. 26, 2026).

[29] Kontex. (2024). X6R: 128-Channel Digital Headstage with HDMI Interface. [Online]. Available: https://docs.kontex.io/Headstage/X6R/X6R128_HDMI/ (Accessed: Jan. 26, 2026).

[30] Cambridge Neurotech. (2024). *Mini-amp-128 Digital Headstage*. [Online]. Available: https://www.cambridgeneurotech.com/headstages (Accessed: Jan. 29, 2026).

Tianyu Bai received the B.S. degree in electrical engineering and mathematics from the University of Missouri, Columbia, MO, USA, in 2019. He is currently pursuing a Ph.D. degree in engineering science at Dartmouth College, Hanover, NH, USA.

His current research focuses on the intersection of microelectronics and neuroscience, specifically in miniaturized hardware implementation, insertion-free interconnect technologies, and the system integration of high-bandwidth neural recording platforms.

Gen Li received the B.E. degree in Thermal and Energy from Tongji University, Shanghai, China, in 2016, the M.S. degree and the Ph.D. degree in Mechanical Engineering from the University of Illinois at Chicago, Chicago, US, in 2017 and 2021.

He is currently a research scientist at Dartmouth College, Hanover, NH, USA. His current research interests include mechanics in neural engineering and the development of next-generation brain-machine interfaces, with a particular focus on polymer-based chronic brain implants.

Yongli Qi received the B.E. degree in Polymer Materials and Engineering from Sun Yat-sen University, Guangdong, China, in 2013, and the Ph.D. degree in Chemistry and Physics of Polymers from Fudan University, Shanghai, China, in 2019.

She is currently a research scientist at Dartmouth College, Hanover, NH, USA. Her current research interests include the development of multifunctional neuroelectronic platforms for neural probing and modulation, with a particular emphasis on decoding brain chemistry.

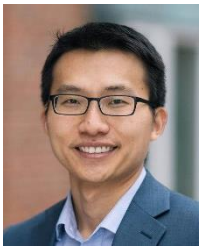

Hui Fang received the B.S. degree in materials science and engineering from Tsinghua University, Beijing, China, in 2009, and the Ph.D. degree in materials science and engineering from the University of California, Berkeley, CA, USA, in 2014.

He is currently an Associate Professor at Dartmouth College, Hanover, NH, USA, where he also serves as the Faculty Director of the Micro and Nano Fabrication Facility. His research focuses on multifunctional materials and devices for large-scale soft microsystem development.

Dr. Fang has received the National Science Foundation CAREER Award and the Thayer Distinguished Research Award for Faculty for his work in neural implant technology.

SUPPLEMENTARY MATERIAL

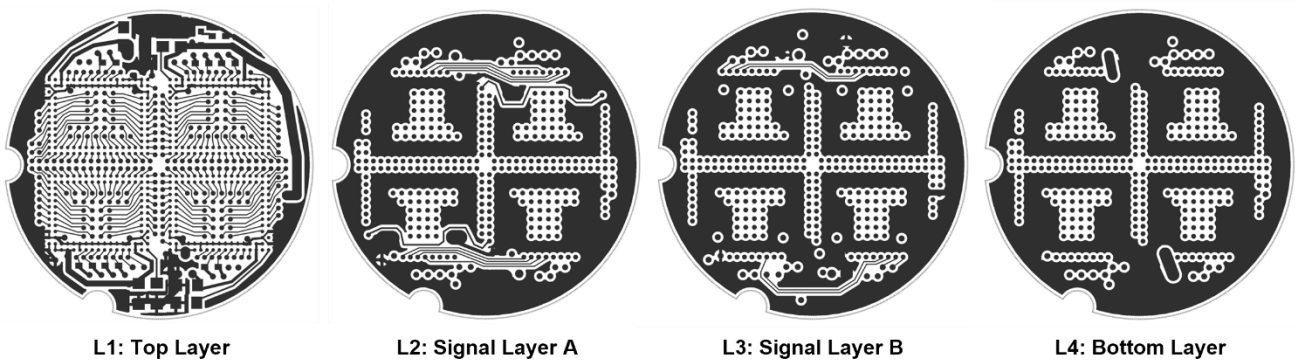

Fig. S1. Layer-by-layer PCB layout of the customized 256-channel headstage. The optimized four-layer stackup manages dense routing of 256 independent channels while ensuring signal integrity. L1 (top) hosts the four symmetrically arranged RHD2164 analog front-end ICs and miniaturized passives. L2 and L3 bury critical high-speed differential SPI communication lines and power (V_{DD}) distribution within grounded copper pours to provide electromagnetic shielding and mitigate digital-to-analog crosstalk. L4 (bottom) serves as a continuous ground plane to provide stable signal return paths and accommodates the high-density BGA footprint for the insertion-free elastomeric interface.

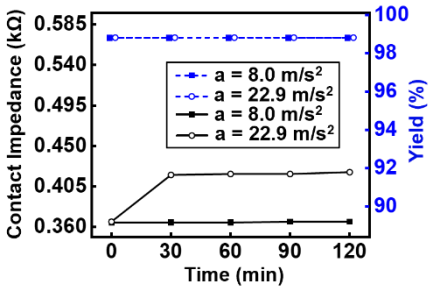

Fig. S2. Dynamic stability and contact impedance drift under simulated motion and micro-vibration. The system demonstrated robust electrical stability over a 120-minute test. Impedance drift was minimal under both 8.0 m/s² (simulating standard dynamic motion) and 22.9 m/s² (simulating extreme micro-vibration) acceleration conditions, and the overall connection yield remained unchanged at 98.8% throughout both testing conditions.